Proceedings of the ASME 2010 3rd Joint US-European Fluids Engineering Summer Meeting and 8th International Conference on Nanochannels, Microchannels, and Minichannels
FEDSM-ICNMM2010
August 1-5, 2010, Montreal, Canada

FEDSM-ICNMM2010-30766

NUMERICAL INVESTIGATION OF THE INFLUENCE OF SIDE WINDS ON A SIMPLIFIED CAR AT VARIOUS YAW ANGLES

Siniša Krajnović*
Division of Fluid Dynamics,
Department of Applied Mechanics,
Chalmers University Of Technology,
SE-412 96 Göteborg, Sweden
Email: sinisa@chalmers.se
http://www.tfd.chalmers.se/~sinisa

Sasan Sarmast

Division of Fluid Dynamics,
Department of Applied Mechanics,
Chalmers University Of Technology,
SE-412 96 Göteborg, Sweden

ABSTRACT

The flow around a generic passenger car under the influence of crosswind was predicted using large eddy simulation (LES). The Reynolds number based on the incoming velocity the car's length, L used was $Re = 9 \times 10^5$. *Yaw angles of crosswind of* 10^o, 20^o *and* 30^o *were studied and the LES results were compared with the experimental observations and previous Reynolds-averaged Naviers-Stokes (RANS) and detached eddy simulations (DES). The present LES were found to predict flows in better agreement with the experimental observations than previous RANS and DES. This shows that LES is better suited than RANS or DES for moderate Reynolds number flows around scale-model car in crosswinds which are inherently unsteady with regions of massive separations.*

*Address all correspondence to this author.

INTRODUCTION

Influence of crosswind on ground vehicles is a result of separated flow on vehicles leeward side and the dynamic behavior of the thereby formed wake. The spectrum of turbulent scales in a wake of vehicle is wide and the flow is unsteady. A detailed experimental investigation or turbulence resolving numerical simulations are the only ways to explore such a flow. Turbulence modeling has shown to be incapable of capturing the complex flow processes of ground vehicles wake and must be excluded in such an investigation (1). The present work uses large eddy simulation (LES) for investigation of the yaw angle influence on the surrounding flow structures.

The objective of the present paper is to document flow processes around a generic passenger vehicle in crosswinds for several yaw angles (between 0^o and 30^o). The emphasis is on the difference in flow physics between two yaw angles where the difference in yaw angle is small (10^o).

Previous work by the first author (2) has

shown that LES is capable of not only accurately predicting flows around generic ground vehicles but also provides a new insight into the unsteady flow physics of such a flow. It is, however, important to be cautious when using LES for ground vehicles especially when separation on the vehicle are not determined by sharp edges. The geometry used in the present work is intended to represent well styled passenger car with no sharp edge separations and the Reynolds number was kept relatively low for the purpose of resolving the near wall flow structures important for an LES. The discussion on LES of wall resolved flows is beyond scope of this article and we refer to work of Krajnović (2; 3) where the resolution issues of bluff body and in particular ground vehicles LES are explained in detail.

1 Previous work

Flows around ground vehicles under influence of crosswinds have been studied in past using both experimental and numerical techniques. Two different kinds of flow effects were studied based on if the yaw angle was kept constant during a trial (4; 5; 6) or if the gusty wind conditions (7; 6; 8) were used. The second kind of study is less common due to difficulties connected with performing experimental or numerical simulations with moving vehicles. Note that some of studies of wind gust influence use continuous change of boundary conditions rather than moving vehicle. However, such an approach implies always simplifications of the real flow conditions. Furthermore, many of the gusty flow situations, such as overtaking or passing of one vehicle (or part of infrastructure such as a train platform) by another vehicle are not possible to consider using such technique.

Probably the first LES of flows around ground vehicles under the influence of crosswinds is that of generic train flows of Hemida and Krajnović (4; 5). Train models in these studies had no sharp edges and the Reynolds number was around 3×10^5 based on the incoming velocity and the train's height. The most important conclusion of (4; 5) is that LES is capable of accurately predicting crosswind flows around smooth surface ground vehicles (at least at moderate Reynolds number). This should be kept in mind as the ground vehicle studied in the present paper has no sharp edges except at its rear and the Reynolds number (based on the vehicle height) is similar to that in (4; 5). Other studies of crosswind effects used more realistic vehicle geometries like that of a bus (6) or a train (7) where separation was often determined by sharp edges. Simulations in (6) and (7) were not LES but detached-eddy simulations (DES) and near wall flow was modeled using turbulence model. LES of flow around realistic ground vehicle geometry in crosswinds has not yet been presented and as discussed in (2) it might be beneficial for a successful LES to include more geometric details of vehicles as that can relax resolution requirements and thereby computational effort for an LES. It is worth mentioning here that the name LES is sometimes misused for unsteady simulations of ground vehicles (which sometimes have very detailed geometry) often at operating Reynolds numbers where only negligible part of turbulent kinetics energy is resolved. Results of such studies are often not validated with more that some global quantity (such as drag) and result of such studies provide no knowledge about performance of LES for ground vehicle flows simply as those simulations are not LES.

2 Description of the generic car and previous investigation

The vehicle studied in the present work was first used in an experimental study of Chometon et al. (9) who used dynamic differential pressure sensors for steady and unsteady pressure measurements. This flow was later simulated of Guilmineau and Chometon (10) with RANS approach and explicit algebraic stress model (EASM). Guilmineau et al. (11) presented also detached eddy simulation of this flow. The results of these two simulations will not be discussed now but we will return to them later when presenting the present LES results. The existence of these RANS and DES simulations together with well documented experimental data makes this flow ideal for evaluation of the capabilities of the present LES simulations. The same geometry was also studied experimentally of Gohlke et al (12) who used Laser Dopler velocimetry (LDV) in addition to force and pressure measurements. However, the Reynolds number in (12) was 2.2×10^6 based on the incoming velocity and vehicles height. Thus the flow is not expected to coincide with that in present LES.

Description of the model

The model is that used in previous experimental and numerical study of Guilmineau and Chometon (10) and Guilmineau et al. (11). The shape of the model is defined according to (10) by combining the two elements:

1. A NACA mean line (A) of chord Ch and geometry factor $a = 1$ with the maximum camber

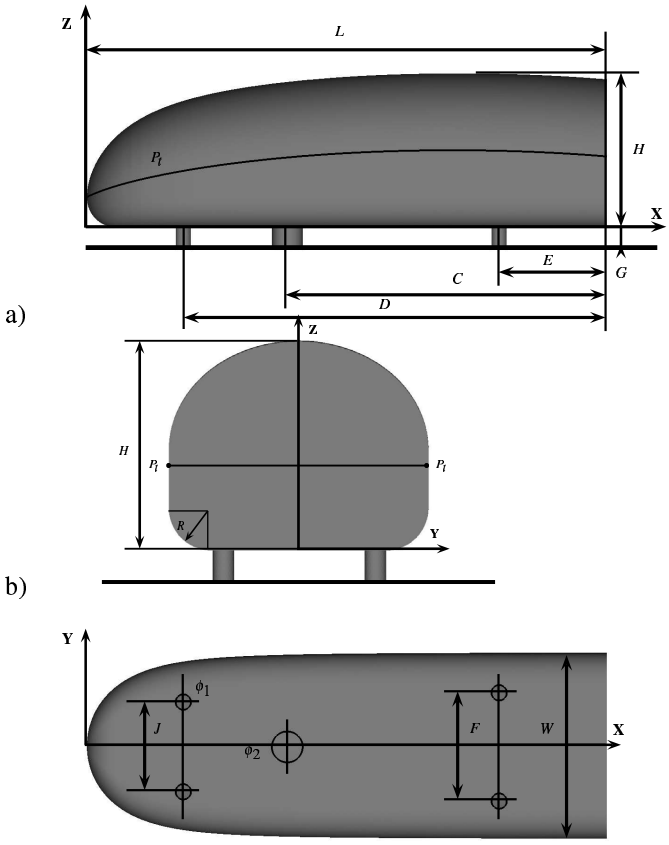

FIGURE 1. Geometry of the body.

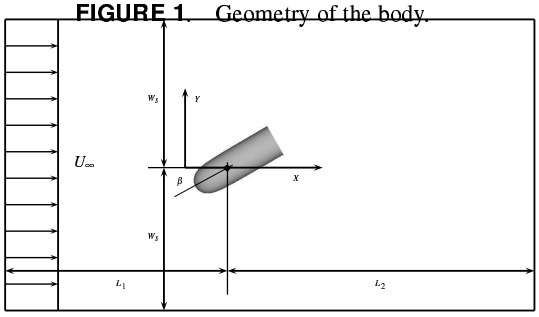

FIGURE 2. Sketch of the models' set-up in the computational domain.

at midchord, $X/Ch = 0.5$. The generic equation of the mean line is

$$Y = 0 \tag{1}$$
$$Z = -\frac{1}{4\pi}\left[\left(1-\frac{X}{Ch}\right) ln\left(1-\frac{X}{Ch}\right) + \frac{X}{Ch} ln\frac{X}{Ch}\right]$$

2. A Rankine half-body with a downstream diameter ϕ.

The geometry of the model can be described using only four parameters, $p_1 = K/\phi$, $p_2 = Lm/L$, $p_3 = Ca/\phi$ and p_4 which is the ratio between the axes of the ellipses of the upper surfaces. Here L is the length of the model , $0.5 < p_2 < 1$, $0 < p_3 < 0.5$and R is defined by $R/L = (1-2p_3)/2p_1$. The parameters used for the model in the present work are $p_1 = 3.3750$, $p_2 = 0.7037$, $p_3 = 0.3050$ and $p_4 = 1.2$. The length of the model is $L = 675$ mm, the width is $W = 240$ mm, the maximum height is $H = 192$ mm and the reference surface is the maximum cross section $S_{ref} = 41.791$ mm. All other dimensions of the model are presented in Table. 1 .

TABLE 1. Dimension of the test model (mm)

C	D	E	F	G	J	K	ϕ_1	ϕ_2
415	550	140	140	29	118	345	20	40

The Reynolds number based on the incoming velocity, U_∞, and the car length, L used in present paper is $Re = 9 \times 10^5$. This is the same Reynolds number as in experimental study of Chometon et al. (9), RANS simulation of Guilmineau and Chometon (10) and DES of Guilmineau et al (11). Three different yaw angles are simulated: 10^o, 20^o and 30^o.

The model is placed in a domain as shown in Fig. 2. The average turbulent intensity at the inlet of the wind tunnel used in the experiments of Guilmineau and Chometon (10) was low (2%). A uniform velocity profile, U_∞, constant in time was thus used as the inlet boundary condition in our LES. The homogeneous Neumann boundary condition was used at the downstream boundary. The lateral surfaces and the ceiling were treated as slip surfaces using symmetry conditions for the lateral sides and the ceiling). No-slip boundary conditions were used on the surface of the body and the channel floor.

Numerical accuracy was established by making two LES on different computational grids containing 6.2 and 9.1, 6.7 and 9.8, and 6.4 and 9.2 million computational nodes, for flow at 10^o, 20^o and 30^o yaw angle, respectively. The computational grids are hexahedral dominated and created using the Fame Hexa automatic mesh generator from AVL Fire. Picture 3 shows the grid with local refinements for the case of yaw angle of 10^o.

The fine computational grid (containing around 9 million nodes) has a wall normal resolution of $n^+ < 0.9$, $9 < \Delta s^+ < 11$ in the streamwise direction and $9 < \Delta l^+ < 11$ in the direction parallel with the surface of the body and normal to the streamwise direction (the mean Δl^+ is around 10). Here $\Delta n^+ = \Delta n \langle u_\tau \rangle_t / \nu$, $\Delta s^+ = \Delta s \langle u_\tau \rangle_t / \nu$,

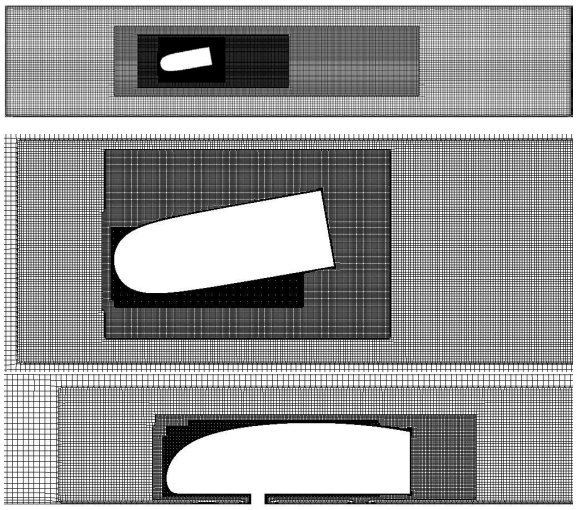

FIGURE 3. Case 10 Degree yaw angle. a) Wind tunnel cut at Z=90 mm, b) Wind tunnel cut at Z=90 mm (zoom) and c) Wind tunnel cut Y=0mm (zoom)

$\Delta l^+ = \Delta l \langle u_\tau \rangle_t / \nu$ and $\langle u_\tau \rangle_t$ is the time-averaged friction velocity. The time step was 1×10^{-4}, giving a maximum CFL number of approximately 0.9. All simulations were first run during time $tU_\infty/H = 166.7$ (16000) until the flow became fully developed. Afterwards, the time-averaging was done during equally long time of $tU_\infty/H = 166.7$.

3 LES Governing Equations

The governing LES equations are the incompressible Navier-Stokes and the continuity equations filtered with the implicit spatial filter of characteristic width Δ (Δ is the grid resolution in this work):

$$\frac{\partial \bar{u}_i}{\partial t} + \frac{\partial}{\partial x_j}(\bar{u}_i \bar{u}_j) = -\frac{1}{\rho}\frac{\partial \bar{p}}{\partial x_i} + \nu \frac{\partial^2 \bar{u}_i}{\partial x_j \partial x_j} - \frac{\partial \tau_{ij}}{\partial x_j} \quad (2)$$

and

$$\frac{\partial \bar{u}_i}{\partial x_i} = 0. \quad (3)$$

Here, $\bar{u}_i$ and $\bar{p}_i$ are the resolved velocity and pressure, respectively, and the bar over the variable denotes filtering.

The influence of the small scales of the turbulence on the large energy carrying scales in Eq. (2) appears in the SGS stress tensor, $\tau_{ij} = \overline{u_i u_j} - \bar{u}_i \bar{u}_j$. The algebraic eddy viscosity model originally proposed by Smagorinsky (13) is used in this paper for its simplicity and low computational cost. The Smagorinsky model represents the anisotropic part of the SGS stress tensor, τ_{ij}, as:

$$\tau_{ij} - \frac{1}{3}\delta_{ij}\tau_{kk} = -2\nu_{sgs}\bar{S}_{ij} \quad (4)$$

where $\nu_{sgs} = (C_s f \Delta)^2 |\bar{S}|$ is the SGS viscosity,

$$\bar{S}_{ij} = \frac{1}{2}\left(\frac{\partial \bar{u}_i}{\partial x_j} + \frac{\partial \bar{u}_j}{\partial x_i}\right) \quad (5)$$

is the resolved rate-of-strain tensor and $|\bar{S}| = \left(2\bar{S}_{ij}\bar{S}_{ij}\right)^{\frac{1}{2}}$. f in the expression for the SGS viscosity is the van Driest damping function

$$f = 1 - \exp\left(\frac{n^+}{25}\right). \quad (6)$$

where n is the wall normal distance. Using this damping function, wall effects are partially taken into account by 'damping' length scale $l = C_s\Delta$ near the walls. The value of $C_s = 0.1$ previously used for bluff-body flows (14) and flow around a simplified bus (15) and generic car called Ahmed body (16) is used in this work. The filter width, Δ, is defined in this work as $\Delta = (\Delta_1\Delta_2\Delta_3)^{1/3}$, where Δ_i are the computational cell sizes in three coordinate directions.

4 Numerical Method

Equations (2) and (3) are discretized using a commercial finite volume solver AVL FIRE for solving the incompressible Navier-Stokes equations using a collocated grid arrangement. Both convective and viscous plus sub-grid fluxes are approximated by a blend of 95% central differences of second-order accuracy and 5% of upwind differences. The time integration is done using the second-order accurate three time level scheme.

Numerical Accuracy

Figure 4 shows pressure coefficient distribution along the curve P_t (Fig. 2) for three different yaw angles of 10^o, 20^o and 30^o and two computation grids for each case. The difference in C_p between the two grids in the present LES results is negligible as seen in Fig. 4. As a second measure of grid convergence, aerodynamic coefficients C_D

and C_S were compared between different grids in Table 2. Difference in drag between two grid simulation is only 0.1%, 1.4% and 1.7% for flows at 30^o, 20^o and 10^o, respectively. Similar comparison for side force coefficients shows only 6%, 0% and 0.4% for flows at 30^o, 20^o and 10^o, respectively. These results together with the near-wall flow resolution presented above which is sufficient for resolving the near-wall structures (important for LES) are proof that computational grids are sufficient for LES.

5 Comparison with the experimental data and previous simulations

Comparison of present LES data was done against the existing experimental data of aerodynamic coefficients and pressure coefficients presented in Guilmineau and Chometon (9). Table 2 shows that the difference in drag varies between 0.5%, 4.5% and 5.6% for 30^o, 20^o and 10^o, respectively. Differences in side force are larger (22%, 20% and 24% for angles between 30^o and 10^o.).

Pressure coefficient along curve P_t for three different yaw angles is compared with the experimental data but also previous RANS (10) and DES (11) simulations in Fig. 5. First observation from this figure is that the C_p values of the present LES agree better with the experimental data than results from previous RANS (10) or DES (11). Agreement of the results of the present LES with the experimental data for 10^o yaw angle is very good and only small under prediction was observed on the leeward side of the body at position around -100 mm. The discrepancy between the LES and the experiments for 20^o yaw angle is slightly larger on the leeward side compared to that for 10^o yaw angle. In particular the difference between the LES results and the experimental data at position -200 mm on the leeward side is rather large (around 16%) for this yaw angle. The difference in C_p between present LES and experiment is largest for 30^o yaw angle. The discrepancy for this angle starts on the leeward side for position of approximately $x = -230$ mm. This discrepancy vanishes at $x = -200$ mm to increase again after approximately $x = -130$ mm. Rather large difference in C_p exists all the way to the rear of the vehicle downstream of this position indicating that the trailing vortex on the leeward side is not accurately predicted for this large yaw angle. Note, however, that present LES prediction is better than previous RANS and DES. This result shows that LES is better suited for prediction of the separation and the resulted wake on the leeward side than RANS or DES.

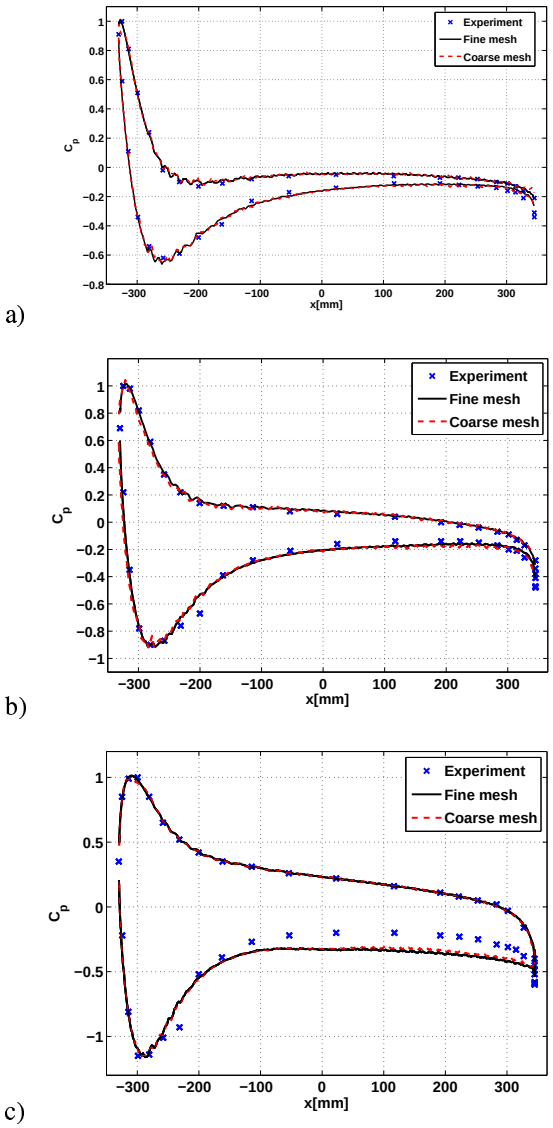

FIGURE 4. Pressure coefficient allong curve (P_t) from the present LES using coarse (dashed line) and fine computational grid (solid line) for a) 10^o, b) 20^o and c) 30^o yaw angle

5.1 Tomography of total pressure coefficients

Tomographies of total pressure coefficients C_{p_i} are drown in x-planes in Figs. 6, 7, 8 and 9. Comparison in these figures was made between the experimental data and present LES prediction as well as previous RANS and DES predictions.

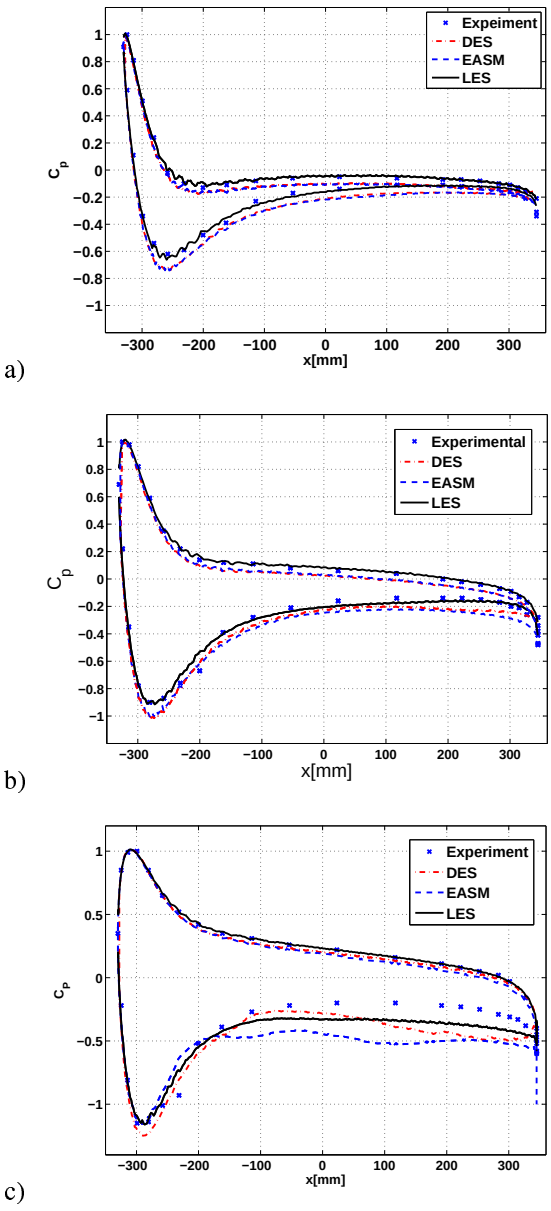

FIGURE 5. Pressure coefficient allong curve (P_t) for present LES and previous RANS (10) and DES (11) for a) 10^o, b) 20^o and c) 30^o yaw angle

At 10^o yaw angle and position $X_o/L = 0.6$, Fig. 6 shows that the boundary layer separation on the leeward side of the model is mainly in the region close to the ground. However, a weak trailing vortex is visible in the upper region of the leeward side. The position $X_o/L = 0.6$ is just behind the rear end of the vehicle. Comparison of the three predictions with the experimental data shows that the RANS simulation predicts too low and too high C_{p_i} behind vehicle and in the large trailing

TABLE 2. Drag and side force coefficients.

Willy Aerodynamic Coefficients	C_D	C_S
Experiment	0.324	-1.21
30 degree Fine	0.3257	-1.4858
30 degree Coarse	0.3261	-1.4564
Experiment	0.378	-0.798
20 degree Fine	0.3949	-0.9556
20 degree Coarse	0.3892	-0.9558
Experiment	0.343	-0.397
10 degree Fine	0.3622	-0.4714
10 degree Coarse	0.3359	-0.4697

vortex near the ground, respectively. The present LES and previous DES predict flows in this plane similar to that in experimental data (6).

Both the upper and the lower trailing vortices become stronger at yaw angle of 20^o as shown in Fig. 7. RANS predicts too high total pressure at the position of the lower trailing vortex for this yaw angle as well. Although there are some similarities between the present LES and previous DES predictions at 20^o, a closer look shows differences. The DES gives more diffused lower trailing vortex of somewhat irregular shape that was not observed in the experiment. Furthermore, the total pressure coefficient is higher at height below the body than in the experiment. This is probably caused by the diffused lower trailing vortex. The LES flow structures are on the other hand in a very good agreement with the experimental observations.

Guilmineau and Chometon (10) reported an over prediction of the vortex intensity for yaw angle 30^o in their RANS simulation which they attributed to the tendency of the solver used in their investigation. The same solver was used in previous DES (10) and this may be the reason of too large total pressure coefficient in DES shown in Figs. 8 and 9. The present LES predicts the intensity of the vortices similar to those found in the experimental observations.

Figures 8 and 9 show the existence of a third vortex close to the ground between the body and the large trailing vortex in the experimental data and all numerical predictions. Although there are differences between the numerical prediction and the experimental data, the LES seems to provide the picture of the flow structures closest to the experimental one.

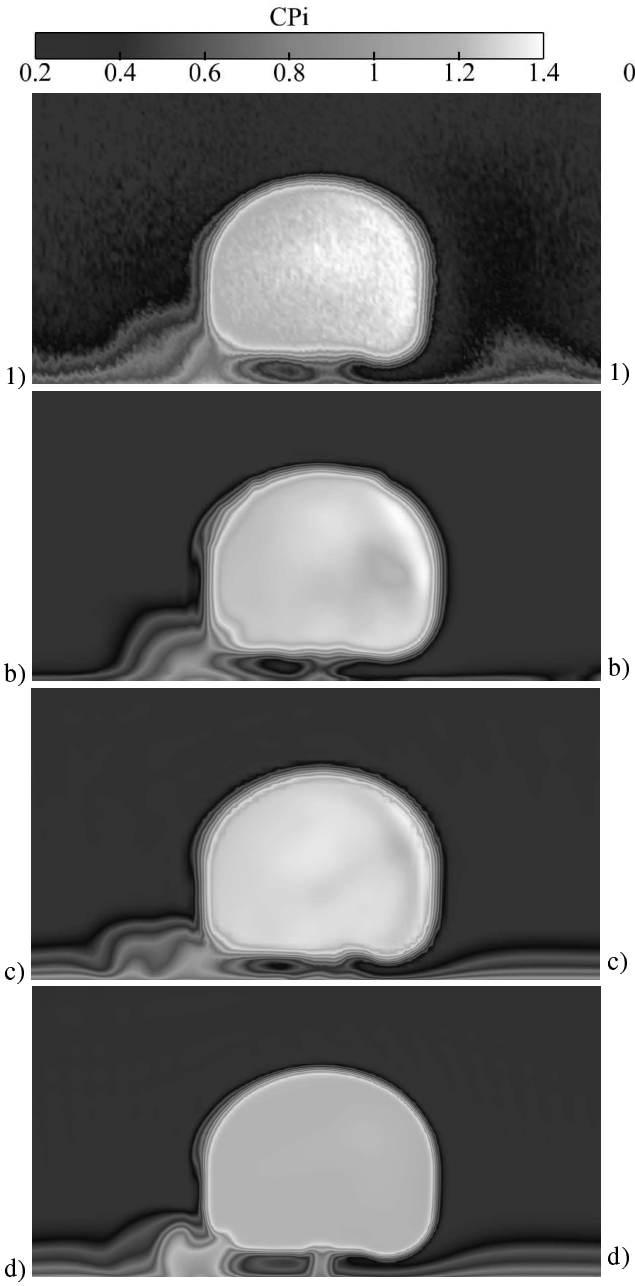

FIGURE 6. Tomographies of total pressure coefficients C_{p_i} for 10^o yaw angle at $X_o/L = 0.6$. a) Experiment; b) LES; c) DES (11); d) RANS (10).

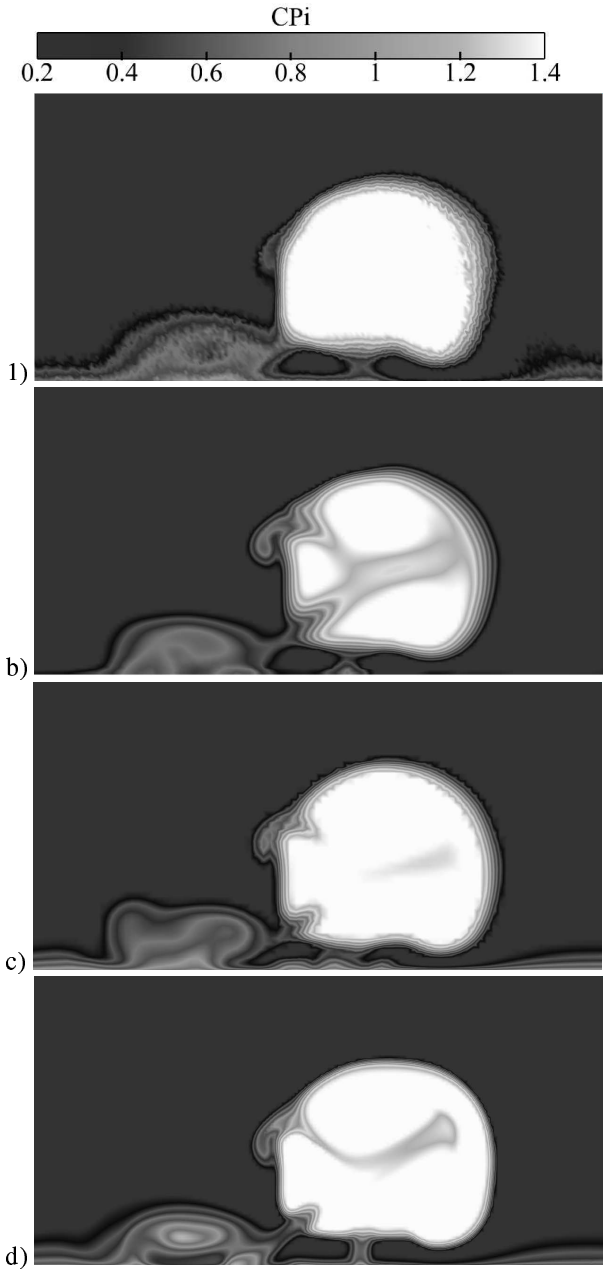

FIGURE 7. Tomographies of total pressure coefficients C_{p_i} for 20^o yaw angle at $X_o/L = 0.6$. a) Experiment; b) LES; c) DES (11); d) RANS (10).

The body of the vehicle is supported by four cylinders and one fifth cylinder is used to protect the pressure tubes. Interaction of these cylinders with the flow results in vortex shedding (Fig. 10). Furthermore, these wakes interact with cylinders downstream. Figure 10 shows the flow below the vehicle for yaw angle 30^o. This vortex shedding averages to the flow shown in Fig. 11. Again the present LES results in the flow in best agreement with the experimental picture. The previous RANS predicts too wide wakes behind cylinders while the total pressure in DES has too low values behind cylinders.

.

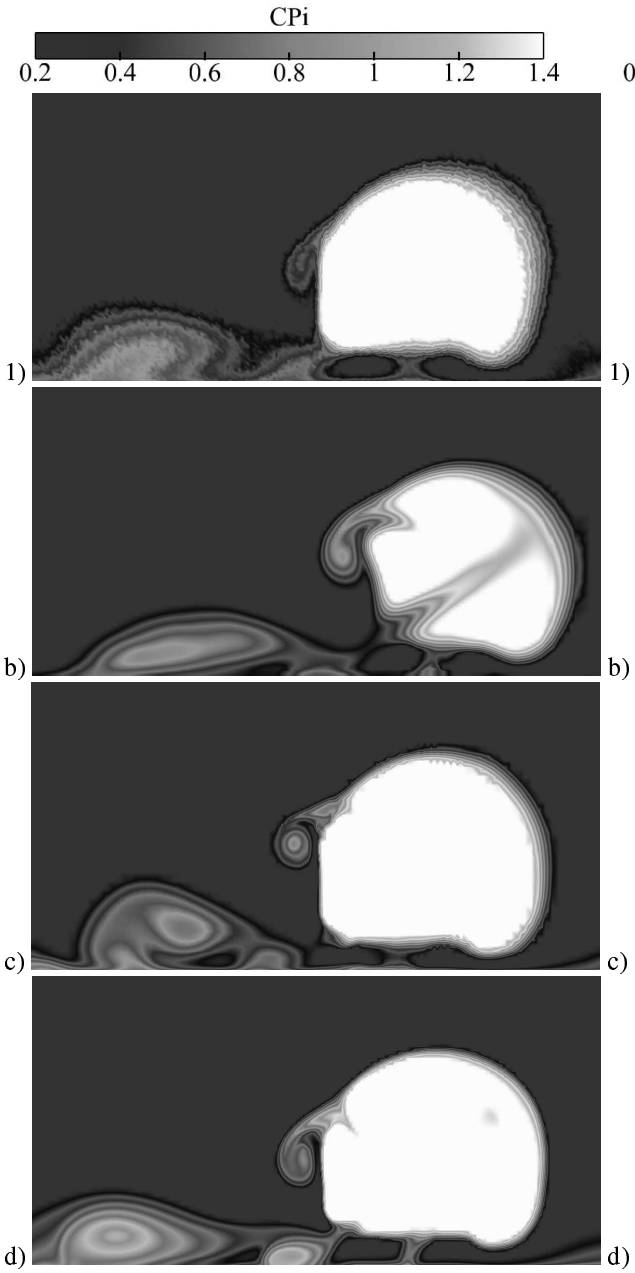

FIGURE 8. Tomographies of total pressure coefficients C_{p_i} for 30^o yaw angle at $X_o/L = 0.55$. a) Experiment; b) LES; c) DES (11); d) RANS (10).

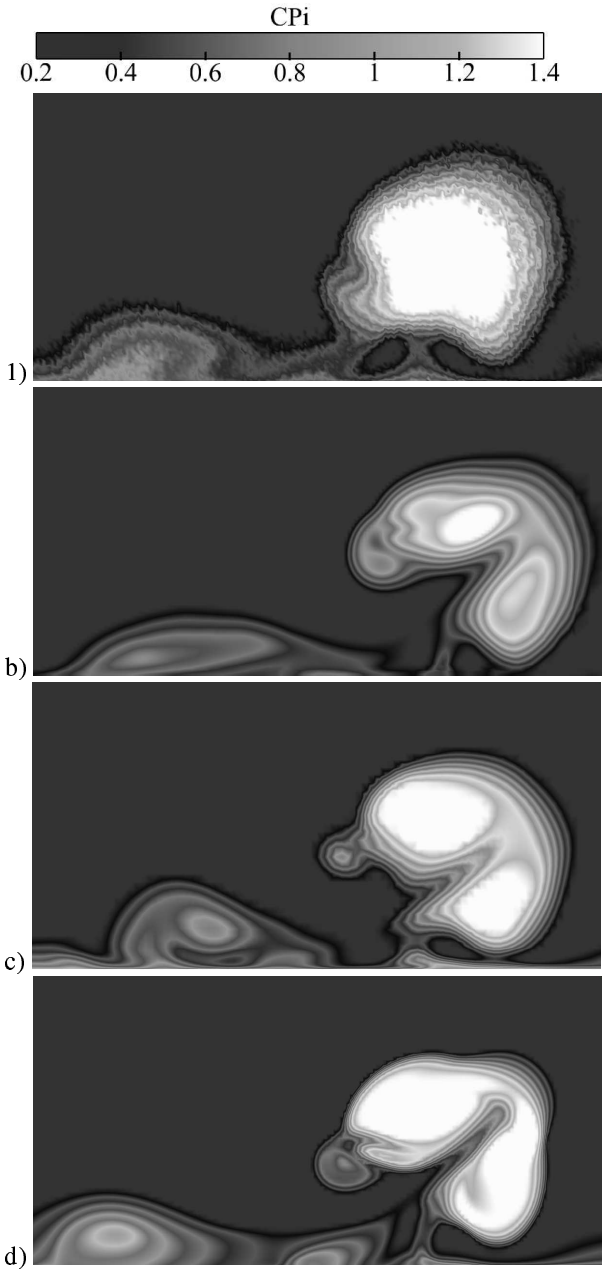

FIGURE 9. Tomographies of total pressure coefficients C_{p_i} for 30^o yaw angle at $X_o/L = 0.65$. a) Experiment; b) LES; c) DES (11); d) RANS (10).

6 Instantaneous flow

One of the reason that LES is better suited for prediction of this flow than RANS is that the flow is inherently unsteady. Figure 12a shows an example of the aerodynamic coefficients for the flow at yaw angle of 20^o. Note that this figures does not show all the computed time steps but only a selection of them. Figure 12b-c shows the difference in the flow structures between the times of $t = 2$s and 2.4s corresponding to times of small and large aerodynamic coefficients, respectively.

Figure 13 shows the corresponding change in flow between two times for the 30^o yaw angle. Larger yaw angle produces wider wake on the leeward side but also stronger interaction between the flow structures behind the vehicle's base with

those on the leeward side of the vehicle. The difference between the minimal and maximal aerodynamic forces shown in Figs. 13a seems to be in much stronger interaction between the base and leeward wakes for the time of maximum forces (compare 13b and 13c, showing flows resulting in minimal and maximal aerodynamic forces, respectively). Figure 13c shows that at position of maximum side and drag forces, the upper trailing vortex becomes stronger and the base wake bends towards the leeward side. Such concentration of the flow structures close to the base left corner shown in Fig. 13 results in strong decrease of surface pressure in Fig. 14b and lower side and drag forces.

7 Discussion

The present work shows that LES is not limited to prediction of flows around ground vehicles with sharp edge separations such as Ahmed body flow (16) but also for flows where separation occurs at surface with curvature. It is important to mention that the Reynolds number in this work is of the order of previous Ahmed body LES and much lower than that of operating conditions of ground vehicles. Furthermore, this prediction capability of LES was shown here only for yawed flows where flow is dominated by regions of separated flow. LES of the flow at zero yaw angle is ongoing but the authors are confident in positive results of this LES since the LES at small yaw angle of 10^o predicted flow accurately. There is still space for improvement in particular at larger yaw angles as shown in mismatch of the LES and experimental curves for pressure coefficient at the leeward side at 30^o yaw angle. The reasons for these discrepancies need to be explored further to find out if they are caused by poor resolution or inadequacy of LES for prediction of this yaw angle. The present results are encouraging as they give hope that transient flow with vehicle rotating around its vertical axes can be studied using LES. The LES approach equips us with a tool to study flow around vehicles under the influence of gusty wind conditions. In particular interesting is to study how small changes in yaw angles (or pitch angle) influence the surrounding flow and resulting aerodynamic forces and moments. Such small changes in vehicles position are common and the resulting aerodynamic reactions interact with the vehicles suspensions and tires influencing vehicles comfort and safety.

ACKNOWLEDGMENT

The authors would like to thank Emmanuel Guilmineau and Michel Visonneau from Centrale Nantes/CNRS in France for providing us with the results of their RANS and DES simulations for comparison with our LES. Thanks go to Dr. Branislav Basara at AVL List GmbH for his technical support regarding the AVL Fire solver during the project. The authors are grateful to AVL List GmbH for providing the licences of Fire AVL solver for the project. Computer time at SNIC (the Swedish National Infrastructure for Computing) at the Center for Scientific Computing at Chalmers (C3SE) is gratefully acknowledged.

REFERENCES

[1] W. Haase, B. Aupoix, U. B., and Schwamborn, D., 2006. *FLOMANIA - A European Initiative on Flow Physics Modelling, Notes on numerical fluid mechanics and multidisciplinary design - Volume 94.* ISBN-10 3-540-28786-8 Springer Berlin Heidelberg New York.

[2] Krajnović, S., 2009. "LES of flows around ground vehicles and other bluff bodies". *Approved for publication in Philosophical Transactions A.*

[3] Krajnović, S., 2002. "Large Eddy Simulations for Computing the Flow Around Vehicles". PhD thesis, Dept. of Thermo and Fluid Dynamics, Chalmers University of Technology, Gothenburg.

[4] Hemida, H., and Krajnović, S., 2008. "LES study of the influence of train nose shape on the flow structures under cross-wind conditions". *ASME: Journal of Fluids Engineering,* ***130***.

[5] Hemida, H., and Krajnović, S., 2008. "Exploring flow structures around a simplified ICE2 train subjected to a 30 degree side wind using large-eddy simulation". *Accepted for publication in the Journal of Engineering Applications of Computational Fluid Mechanics.*

[6] Hemida, H., and Krajnović, S., 2008. "Transient simulation of aerodynamic response of a double-deck bus in gusty winds". *Accepted for publication in the ASME: Journal of Fluids Engineering.*

[7] Krajnović, S., 2009. "Shape optimization of high-speed trains for improved aerodnamic performance". Journal of Rail and Rapid Transit, Vol 223, No F5, pp. 439-452.

[8] Krajnović, S., Bjerklund, E., and Basara, B., 2009. "Simulation of the flow around high-

speed trains meeting each other and at the exit of a tunnel".

[9] Chometon, F., Strzelecki, A., Ferrand, V., Dechipre, H., Dufour, P., Gohlke, M., and Herbert, V., 2005. "xperimental study of unsteady wakes behind an oscillating car model.". In SAE Technical Paper No. 2005-01-0604.

[10] Guilmineau, E., and Chometon, F., 2009. "Effect of side wind on a simplified car model: Experimental and numerical analysis". *ASME: Journal of Fluids Engineering,* ***131***.

[11] Guilmineau, E., Chikhaoui, O., Deng, G., and Visonneau, M., 2009. "Effect de vent lateral sur un modele simplifie de voiture par une methods des". *Mecanique & Industries,* ***10***, pp. 203–209.

[12] Gohlke, M., Beaudoin, J. F., Amielh, M., and Anselmet, F., 2007. "Experimental analysis fo flow structures and forces on a 3d-bluff-body in constant cross-wind". *Experiments in Fluids,* ***43***, pp. 579–594.

[13] Smagorinsky, J., 1963. "General circulation experiments with the primitive equations". *Monthly Weather Review,* ***91***(3), pp. 99–165.

[14] Krajnović, S., and Davidson, L., 2002. "Large eddy simulation of the flow around a bluff body". *AIAA Journal,* ***40***(5), pp. 927–936.

[15] Krajnović, S., and Davidson, L., 2003. "Numerical study of the flow around the bus-shaped body". *ASME: Journal of Fluids Engineering,* ***125***, pp. 500–509.

[16] Krajnović, S., and Davidson, L., 2005. "Flow around a simplified car, part 1: Large eddy simulation". *ASME: Journal of Fluids Engineering,* ***127***, pp. 907–918.

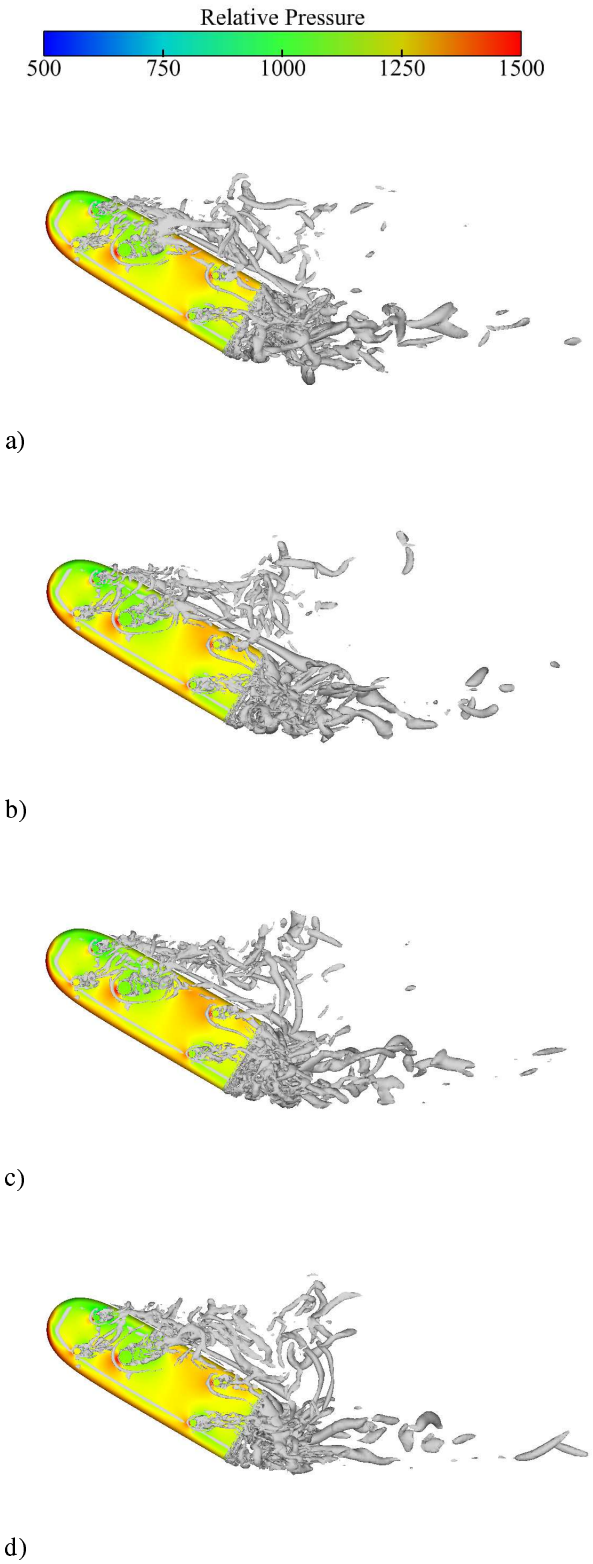

FIGURE 10. An isosurface of the second invariant of the velocity gradient Q for flow at yaw angle 30^o. Pictures are corresponding times a) 2.9 s, b) 2.5 s, c) 2.3 s and d) 1.8 s. View is from below. Figures (a) and (d) represent the flow at minimum and maximum drag, respectively.

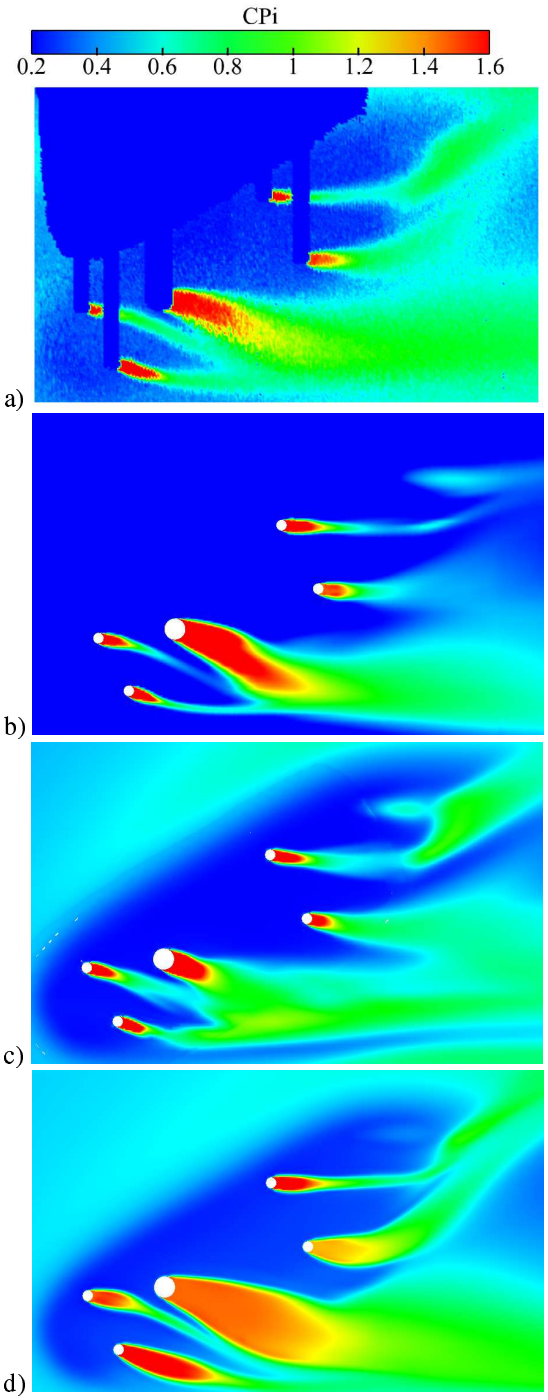

FIGURE 11. Tomographies of total pressure coefficients C_{p_i} for 30^o yaw angle at at Z=0.0145. a) Experiment; b) LES; c) DES (11); d) RANS (10).

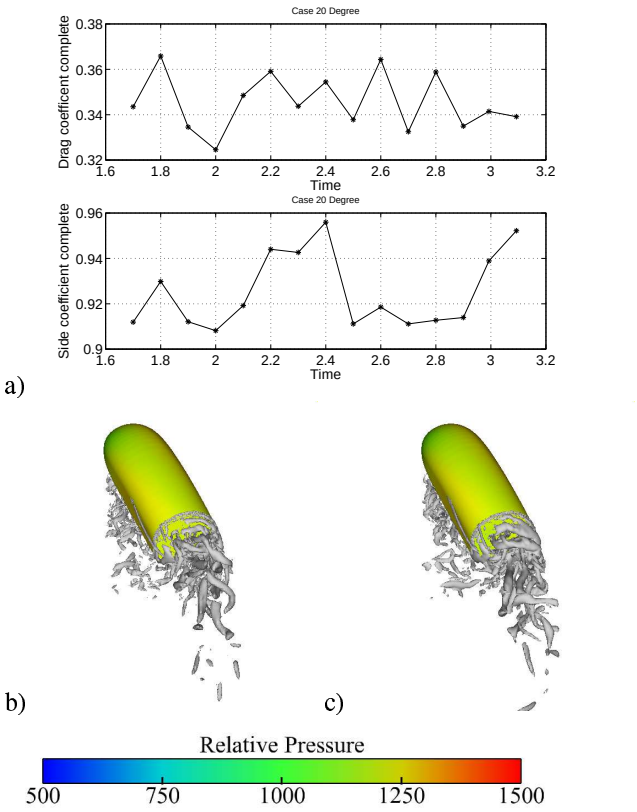

FIGURE 12. Yaw angle of 20^o. a) Drag and side force coefficients for sample of time steps. b) Second invariant of the velocity gradient Q at times $t = 2$ s and $t = 2.4$ s.

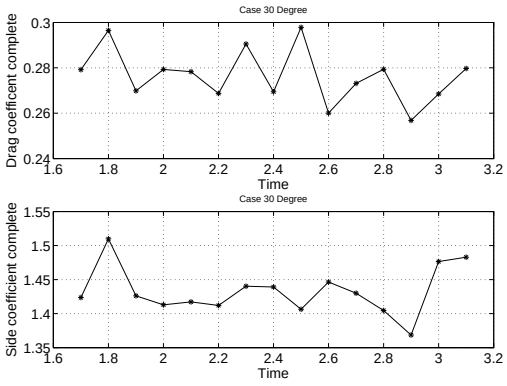

a)

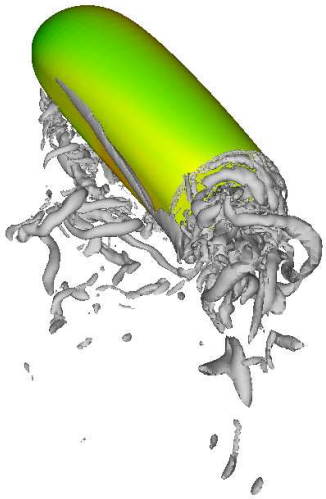

b)

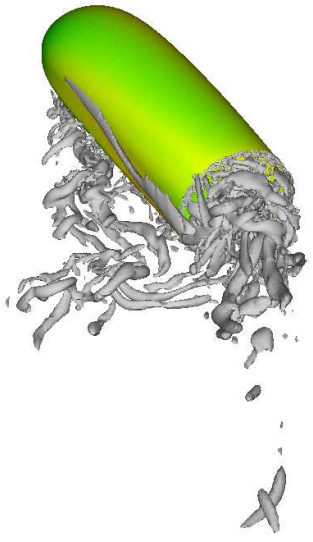

c)

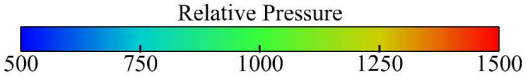

FIGURE 13. Yaw angle of 30^o. a) Drag and side force coefficients for sample of time steps. b) Second invariant of the velocity gradient Q at times $t = 2.9$ s and $t = 1.8$ s.

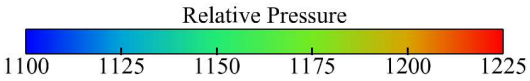

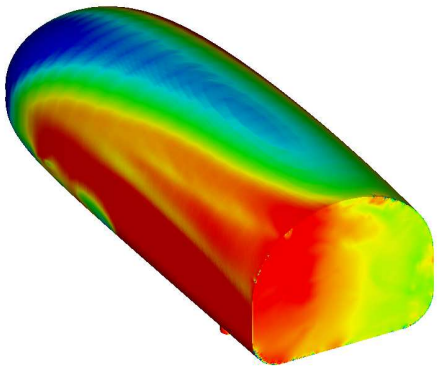

a)

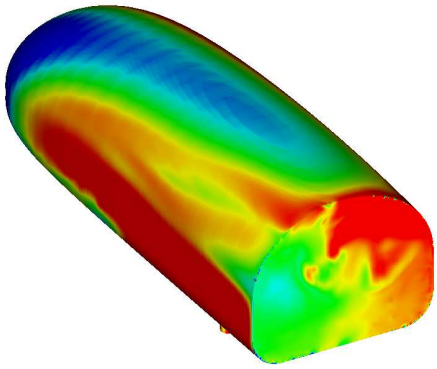

b)

FIGURE 14. Yaw angle β=30^o: Surface pressure (rear isometric view) at times a) $t = 2.9$ s and b) $t = 1.8$ s..